JOURNAL OF AIRCRAFT
Vol. 30, No. 6, Nov.–Dec. 1993

Euler Code Prediction of Near-Field to Midfield Sonic Boom Pressure Signatures

M. J. Siclari*
Grumman Corporate Research Center, Bethpage, New York 11714
and
C. M. Darden†
NASA Langley Research Center, Hampton, Virginia 23665

A new approach is presented for computing sonic boom pressure signatures in the near field to midfield that utilizes a fully three-dimensional Euler finite-volume code capable of analyzing complex geometries. Both linear and nonlinear sonic boom methodologies exist, but for the most part rely primarily on equivalent area distributions for the prediction of far-field pressure signatures. This is due to the absence of a flexible nonlinear methodology that can predict near-field pressure signatures generated by three-dimensional aircraft geometries. It is the intention of the present study to present a nonlinear Euler method that can fill this gap and supply the needed near-field signature data for many of the existing sonic boom codes.

Introduction

MUCH of the existing sonic boom prediction and optimization methods are based on the modified linear theory analysis originated by Whitham[1] and extended by Walkden[2] for lifting bodies. The linear methods have also been modified to include the effects of a stratified atmosphere.[3] Other methods have included a nonlinear Euler analysis using a modified method of characteristics that approximately accounts for three-dimensional effects.[4–7]

Several experimental studies[8] and analytical studies[9] have questioned the validity of linear methods in both analysis and design of configurations for low sonic boom as the freestream Mach number approaches 3. In the higher Mach number regime, strong shocks are generated which have significant higher order entropy production. These effects are totally neglected by the linear methods. These higher order terms are addressed by the quasiaxisymmetric nonlinear modified method of characteristics (MMOC).[4–7] The drawback to the MMOC method is that it requires nonlinear near-field initial data to compute the far-field solution. The near-field initial data could be acquired by wind-tunnel tests. This is an expensive solution, and it is not clear whether wind-tunnel tests could even supply all of the needed parameters such as pressure, flow angularity, velocities, shock angles, etc., required by the nonlinear code.

In the last decade, computational fluid dynamics (CFD) has matured tremendously due to the simultaneous development of fast algorithms to solve nonlinear flow equations and the tremendous advances in computer technology. The high-speed flow about complex three-dimensional geometries representative of realistic aircraft can now be computed in a matter of minutes on present day supercomputers with grids containing from 100,000 to 500,000 mesh points. One such method to solve the Euler equations for high-speed flows is documented in Refs. 10 and 11. This method uses a central difference finite volume method in the crossflow planes, and an implicit upwind finite difference technique in the marching direction to solve the three-dimensional unsteady Euler equations. An explicit multistage Runge-Kutta time integration with local time stepping and residual smoothing is used to solve for the steady-state solution.

It is the intent of the present study to present a modification of the aforementioned finite volume Euler methodology that will be capable of computing near- to midfield sonic boom pressure signatures as input to the nonlinear sonic boom codes for far-field predictions.

The three-dimensional unsteady Euler equations are written in a physical space conical/spherical coordinate system. For three-dimensional supersonic flows, the present technique utilizes an upwind marching on spherical surfaces. The upwind treatment of the marching terms has the advantage of not requiring added dissipative terms in the marching direction. Employing spherical surfaces for marching allows the treatment of lower freestream Mach numbers prior to encountering subsonic Mach numbers in the marching direction. This is essential for the computation of wings in the lower supersonic Mach number regime. The marching is fully implicit in that the nonconical terms are included in each stage of the Runge-Kutta integration scheme. Therefore, a pseudotime integration is employed to converge to a steady-state solution for each crossflow plane. This essentially eliminates all marching step size stability constraints, except those dictated by accuracy requirements.

The three-dimensional implicit marching method treats the crossflow terms in a similar fashion to the conical flow method by using a conical coordinate finite volume scheme in physical space. The three-dimensional terms are evaluated separately in a computational space in finite difference form. This, in essence, yields a hybrid method which utilizes the salient features of the explicit, unsteady, physical space, finite volume method for each crossflow plane with a simple finite difference upwind treatment for the marching terms. Details of the computational procedure can be found in Refs. 10 and 11. This method has developed into a code called multigrid implicit marching (MIM3D).

Grid Topology for Sonic Boom Signature Computations

The standard grid topology for the supersonic marching Euler code MIM3D is to use stacked crossflow plane grids as the computation proceeds downstream on the vehicle. The outer boundary of these grids is taken far enough away from

Presented as Paper 90-4000 at the AIAA 13th Aeroacoustics Conference, Tallahassee, FL, Oct. 22–24, 1990; received March 5, 1991; revision received Sept. 18, 1992; accepted for publication Sept. 25, 1992.

*Laboratory Head. Associate Fellow AIAA.
†Aerospace Technologist. Associate Fellow AIAA.

the surface to capture the bow and embedded shock waves. Several modifications to this procedure were necessary to accurately predict sonic boom signatures at distances normal to the aircraft centerline on the order of one body length and beyond.

At Mach numbers 2, 3, and 4, the computation must march approximately 3, 4, and 5 body lengths, respectively, downstream of the nose of the vehicle just to be able to compute a height normal to the aircraft axis of just one body length. As the procedure marches downstream of the aircraft, the distance between the bow shock and aircraft axis increases. If the same number of mesh points are used, the resolution of the flowfield decreases as the computation proceeds downstream. To alleviate this problem, a unique approach is used and is illustrated in Fig. 1, which shows a typical mesh topology for an axisymmetric projectile. Figure 1 shows the shape of the projectile, the two symmetry planes, and a typical crossflow plane mesh. The base of the vehicle is typically extended about one body length to approximate a sting. The surface of the grid is then flared out at the Mach angle of the freestream Mach number. The usual surface boundary condition of flow tangency is applied on the surface of the vehicle and the base sting extension. On the Mach cone extension, freestream pressure without flow tangency is applied, effectively extrapolating the characteristics. The boundary conditions on the Mach cone will not affect the flowfield if the body extension is long enough so that the base shock does not interact with the Mach cone surface.

Another modification to the grid is required as the distance of the signature increases from the aircraft axis. For example, at Mach 3, if a signature is required at 3 body lengths normal to the model axis, the computation must compute downstream to an axial distance of approximately 9 body lengths. For this type of computation, it is difficult to, a priori, prescribe the shape of the outer boundary to keep the bow shock within this boundary and approximately parallel to it. Two adverse effects can occur. The bow shock may intersect the outer boundary which essentially negates the validity of the computation, or the outer boundary angle is greater than the local shock angle and the bow shock travels downward through the grid. This results in a loss of resolution and accuracy since the mesh points lying outside of the bow shock are at freestream values. To correct this problem, the outer boundary is adapted to the bow shock by detecting the location of the bow shock in the grid and moving the grid at each axial station to keep the bow shock within a specified number of points from the outer boundary. This boundary adaptation becomes critical at the higher Mach numbers, such as 3 and 4, since the bow shock angle at the nose may be 30 to 40 deg and the Mach angle is only 20 to 15 deg. Several examples of this boundary adaptation will be shown in the next section.

In order to be able to compute the flow several body lengths downstream of the projectile or aircraft, a constant axial step size would require the use of an inordinate amount of points. To alleviate this problem, the grid is stretched in the axial direction aft of the surface of the object. Typically, the grid stretching is commenced on the sting with the use of a constant step size growth factor. Hence, the axial step size continually increases until, at the end of the computation or far downstream, the step size may be on the order of a body length. The decay of the pressures is asymptotic in the sense that the pressure decays rapidly in the near field and then the rate of decay becomes more and more gradual as the far field is approached, allowing for much greater axial step sizes without loss of accuracy.

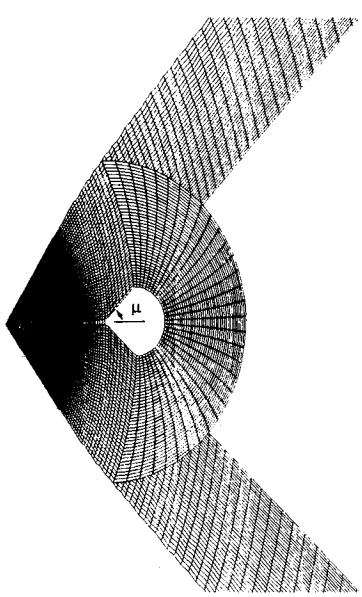

Fig. 1 Basic grid topology used for sonic boom computations.

Simple Axisymmetric Projectiles

Boundary Adaptation

Several comparisons between predicted sonic boom pressure signatures and measured wind-tunnel data will be presented for a variety of shapes. Figure 2 shows the computed pressure pattern on a (41 × 64) crossflow mesh by 156 axial stations for an axisymmetric projectile with a sting extension at the base at $M = 2.01$ and 0 angle of attack. The surface of the body is computed with 56 stations, leaving 100 stations to be used to compute the downstream flow with a moderate axial stretching constant of 1.05. A stretching constant of 1.05 allows for a 5% growth in each axial marching step downstream of the body.

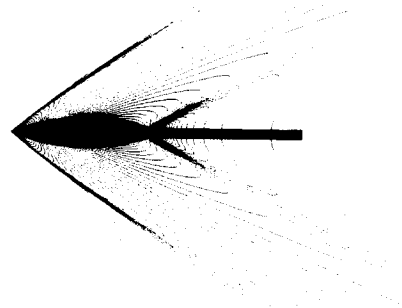

Fig. 2 Computed pressure pattern for an axisymmetric projectile at $M_\infty = 2.01$ and $\alpha = 0$ deg.

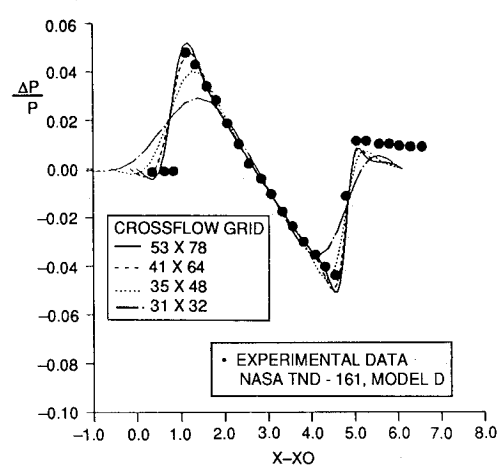

Fig. 3 Computed pressure signatures for an axisymmetric projectile at $M_\infty = 2.01$, $\alpha = 0$ deg at $H/L = 8$ as a function of crossflow mesh density.

The captured bow shock and base shock can be clearly seen in Fig. 2. The reason for the long extension of the base can also be seen since the recompression on the sting surface interacts with the tail shock. The sting extension will not affect the tail shock as the angle of the base shock approaches the local Mach angle coming from the end of the base extension. Unfortunately, it is difficult to predict this interaction, a priori, and experience has led to a minimum sting length of one body length in the computation. In experiments, the shape of the sting will have an effect on the strength of the base shock and should be modeled correctly in the computation. Unfortunately, details of the sting geometry are not readily available in the literature, and in the present computations the sting was always assumed to be cylindrical.

Figure 3 shows the effect of crossflow mesh resolution on the computed pressure signature in comparison with the measured data of Ref. 12 at 8 body lengths normal to the axis of the axisymmetric projectile of Fig. 2. Both computed and experimental signature lengths were referenced to 0, as noted by the abscissa x-x_0, for comparison purposes. The experimental data was obtained using pressure taps located on a flat plate. A reflection factor of 1.8 was used in the computed results in order to account for the shock reflection and compare with the test data. The mesh resolution in the crossflow plane has a pronounced effect on the accuracy of the solution as compared to the measured data because of the shock capturing scheme. At least 64 points normal to the surface is needed to accurately predict the shock strengths in the midfield even with the enhanced resolution achieved with the outer boundary adaptation and the Mach cone surface. It should be noted that this sensitivity is marked less pronounced in the near field.

Figure 4 shows the effect of axial resolution on accuracy using the (41 × 64) crossflow mesh. Axial steps of 200, 156, and 121 corresponding to growth constants of 1.025, 1.05, and 1.10 were used for comparison. Only a small effect in accuracy is seen at the lowest resolution. The 121 grid corresponds approximately to half of the axial steps used on the body and the other half used downstream to approximately 15 body lengths. Good accuracy is achieved in the marching direction even for low resolution because of the implicit nature of the scheme. An explicit marching scheme might require a thousand steps or more for the same accuracy.

Figure 5 shows an overall comparison between experimental measurements and computed pressure signatures at distances of H = 1, 2, 4, and 8 body lengths normal to the centerline of this projectile. The (41 × 64 × 156) grid was used for these comparisons. At body lengths of 1, 2, and 4,

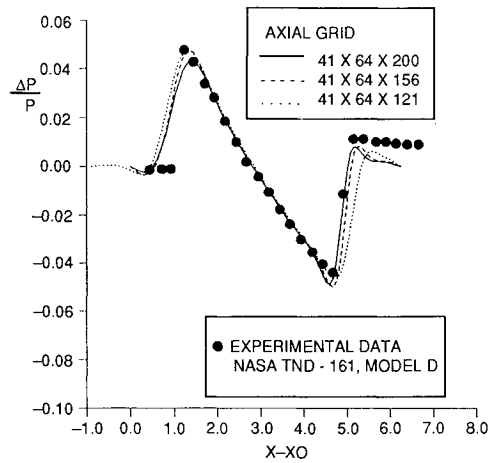

Fig. 4 Computed pressure signatures for an axisymmetric projectile at M_∞ = 2.01, α = 0 deg at H/L = 8 as a function of axial mesh density.

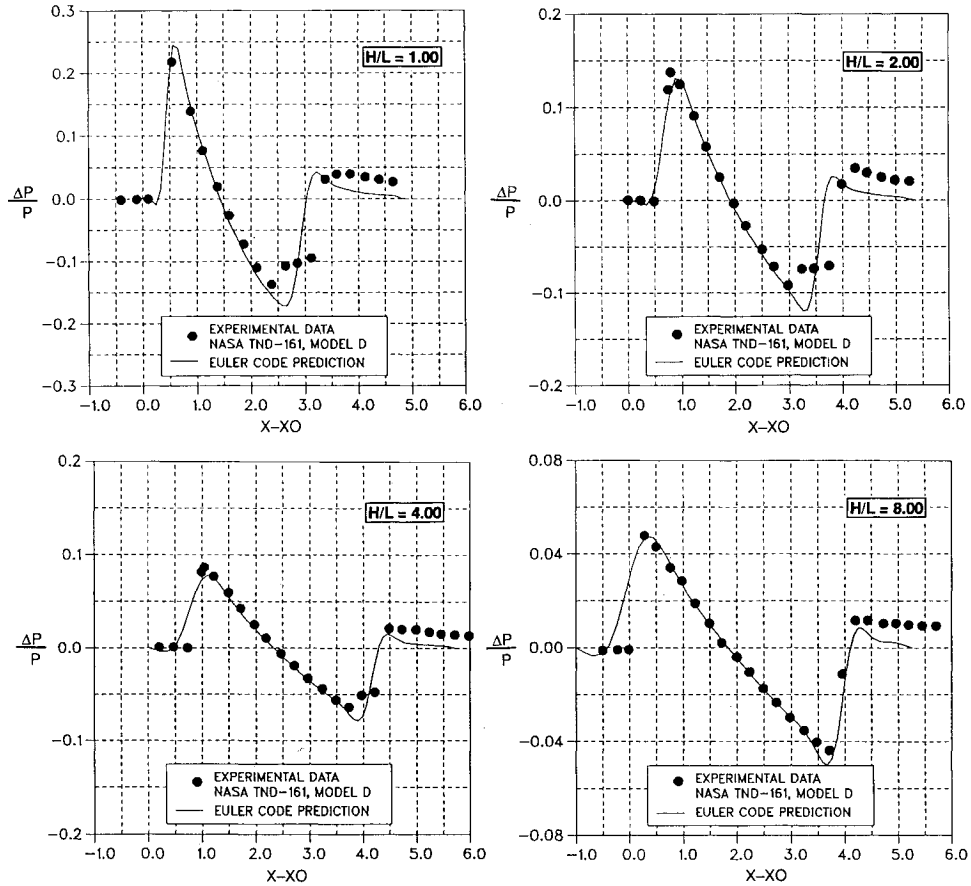

Fig. 5 Comparison of computed pressure signatures with experimental data for an axisymmetric projectile at M_∞ = 2.01 and H/L = 1, 2, 4, and 8.

the correlation is good except for the base shock. A multiple compression is shown by the experimental data in the region of the base shock which could be indicative of separated flow at the base. At 8 body lengths, both signatures indicate a typical N-wave pattern. Excellent correlation between experimental and computed results are indicated. In general, the bow shock overpressure agrees well with the experimental data for all distances from the body.

Grid Adaptation

The previous computations adapted both the outer boundary and inner surface in order to conserve grid points and enhance the accuracy of the present shock capturing scheme. A further advance to this approach would be to adapt the internal grid structure to the flow pattern. Clustering points in the vicinity of shocks would entail fitting the mesh to the shock system. One example of a solution adaptive grid procedure is presented in Ref. 13 and implemented for an upwind parabolized Navier-Stokes solver. The grid adaptation procedure used in Ref. 13 is based on basic techniques presented in Refs. 14 and 15. This grid adaptation procedure is based on an error equidistribution method represented by

$$W_i \Delta S_i = K \tag{1}$$

where W_i is the weighting function, S_i is the computational grid interval, and K is a force constant. W_i is made proportional to a normalized flow property derivative such as pressure, or

$$W_i = 1 + AF_i(\delta p, \delta^2 p) \tag{2}$$

In the present application, F_i is made proportional to the first and second derivatives of pressure. Summing both sides of Eq. (1) leads to the following expression for the new grid intervals ΔS_i, or:

$$\Delta S_i = S_{\max} \Big/ \left(W_i \sum_{n=1}^{N} \frac{1}{W_n} \right) \tag{3}$$

where $S_{\max}$ is the total length of the coordinate line. For sonic boom applications, Eq. (3) is applied along a coordinate line normal to the surface. This cluster points in the vicinity of the outgoing shock waves. Figure 6 shows an example of a solution adaptive grid computed using Eq. (3) locally in a one-dimensional fashion along coordinate lines normal to the surface of the body. Figure 6 illustrates the way in which the grid mimics the shock pattern of the final solution. The present scheme implements the grid adaptation by first projecting the grid computed on the previous axial station to the new station, converging the solution to a specified tolerance, and then readapting the grid and further converging the solution to the final tolerance. This procedure demands more computational time to implement. Figure 6 shows both the near-field and midfield adapted grids. The adaptation persists in the midfield as the shock strengths become very weak due to the normalization of the pressure derivatives at each station. There are still problems to be studied in the implementation of a solution adaptive grid with respect to multiple complex shock systems of differing strengths. The error equidistribution method will naturally yield the most adaptation in the grid to the strongest shock in a multiple shock system because it represents the largest error. Figure 7 shows the computed solution adaptive grid pressure pattern on a (41 × 64 × 156) mesh. This is the same mesh used in Fig. 2. The definition of the shocks is somewhat improved with the grid adaptation. Figure 8 shows a comparison of the computed pressure signatures for the boundary adaptive and the full grid adaptation method in comparison to the experimental data for the axisymmetric projectile of Ref. 12 at $M = 2.01$. Better shock resolution is achieved with the full grid adaptive scheme. It was thought that cruder grids or less resolution could be used with the grid adaptation method. In preliminary computations it was determined that the effects of crossflow mesh resolution depicted by Fig. 3 held true also for the adapted grid solutions. Evidently, a minimum resolution is still needed to resolve the overall flowfield. In the following section, the full grid adaptation method was not implemented for the computation of aircraft flowfields. The implementation of the grid adaptation scheme needs further study before application to a complex aircraft flowfield where several shocks and expansion regions develop and coexist.

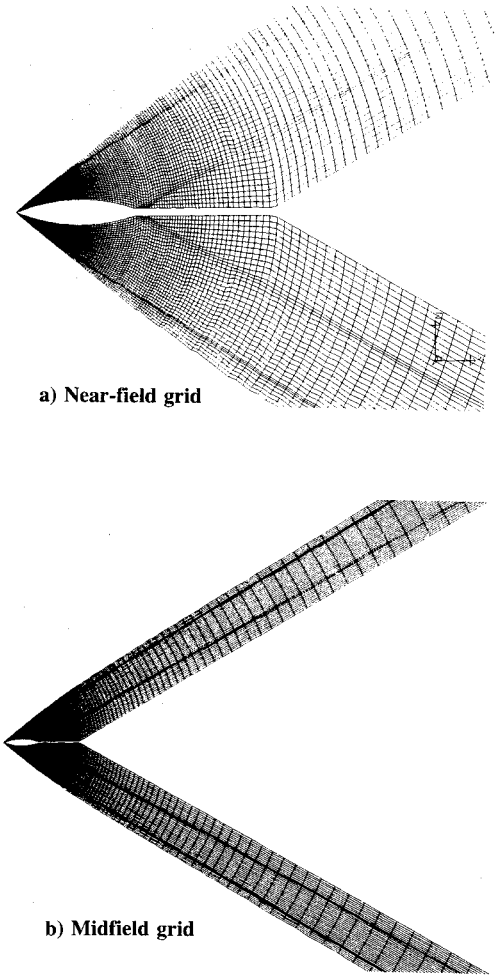

Fig. 6 Example of a solution adaptive grid for an axisymmetric projectile at $M_\infty = 2.01$ and $\alpha = 0$ deg.

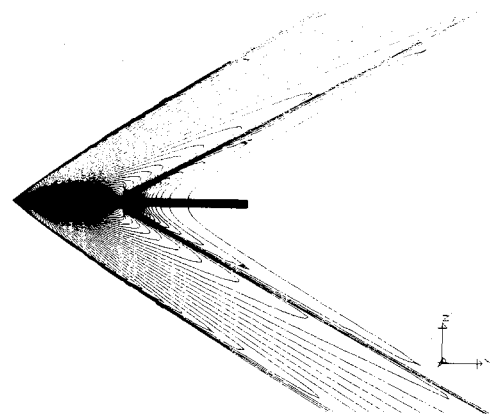

Fig. 7 Computed near-field pressure pattern on a solution adaptive grid for an axisymmetric projectile at $M_\infty = 2.01$ and $\alpha = 0$ deg.

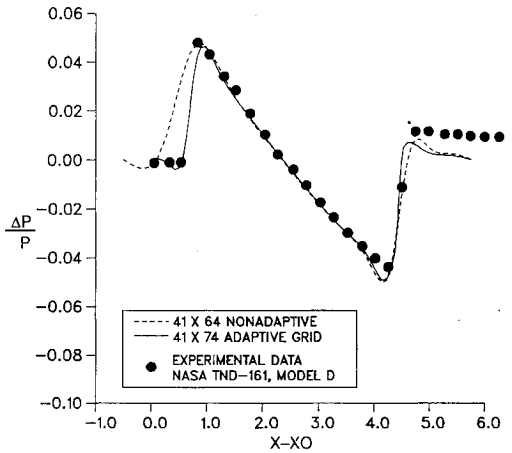

Fig. 8 Comparison of computed pressure signatures with experiment for boundary adaptive and solution adaptive grids for an axisymmetric projectile at $M_\infty = 2.01$, $\alpha = 0$ deg at $H/L = 8$.

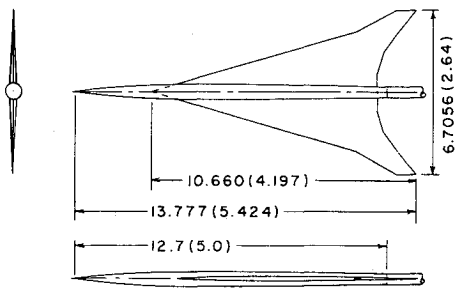

a) Reference arrow wing-body model

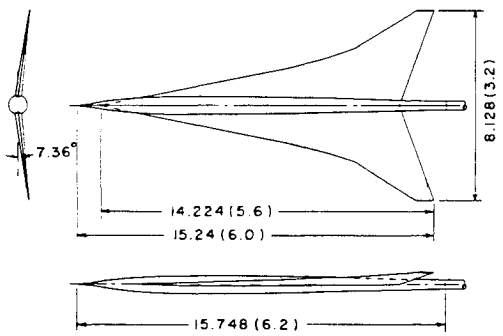

b) Low-boom arrow wing-body model

Fig. 9 Schematic of arrow wing-body scale models[8] dimension in cm (in.).

Aircraft Computations

In Ref. 8, probe measurements of pressure signatures were taken in a wind tunnel for four different aircraft models. The models were small, being about 6 in. in length or about $\frac{1}{600}$ scale. Signature predictions for two of these configurations are included in this article, the reference and the low-boom arrow wing-body models. Both of these models were tested at Mach 2.7. Figure 9 shows a sketch of the two wind-tunnel models. The reference arrow wing-body configuration was symmetric and slightly smaller in size. The low-boom model is longer with a full scale length of 300 ft and has a larger wing with dihedral. The low-boom model was specifically designed to achieve low-boom signatures based on sonic boom minimization theory. The reference configuration was tested at 2.75 deg of incidence and the low-boom model at 2 deg.

Figure 10a shows the near-field pressure contour for the reference arrow wing-body configuration at $M = 2.70$ and $\alpha = 2.75$. A relatively fine crossflow mesh of (85 × 76) was used in the computation with an axial step growth factor of 1.05 aft of the configuration. The reason for the fine mesh will become evident in subsequent paragraphs. The bow shock

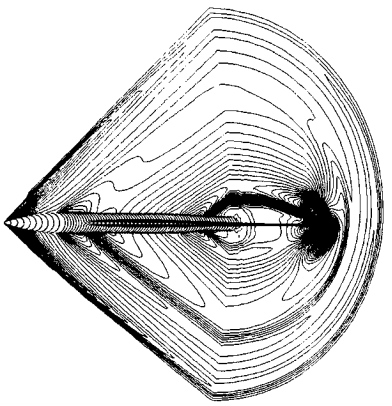

a) $M = 2.7$ and $\alpha = 2.75$ deg

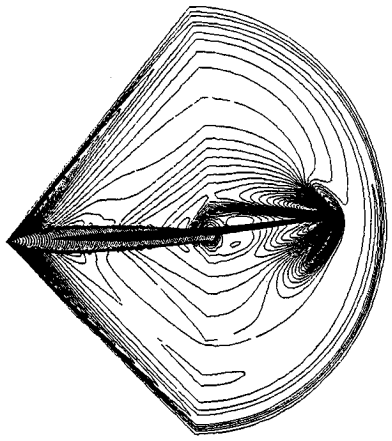

b) $M = 2.7$ and $\alpha = 2$ deg

Fig. 10 Near-field computed pressure pattern for reference and low-boom arrow wing-body configurations.

and wing emergence shock are readily evident on the windward side. The boat tail shock generated by the sting attachment is seen in both planes. The wing trailing edge shock, readily evident on the lee side of the configuration, quickly merges with the sting shock. The wing crank shock is also shown wrapped around the leading edge of the wing in the crossflow plane. The wing crank shock does not seem to wrap around to the symmetry planes, except possibly as a compression.

Figure 10b shows a similar isobar plot for the low-boom arrow wing-body configuration at $M = 2.70$ and $\alpha = 2$ deg. The low-boom fuselage is more contoured and has a spike or cusped-like nose. Two shocks occur near the nose which quickly merge into a single shock. The more highly swept wing diminishes the wing emergence shock. The sting, wing trailing, and wing crank shocks are all evident in the computed pressure pattern of Fig. 10b.

The stronger windward wing emergence shock of the reference configuration is not evident. The low-boom model shows a relatively clean windward pressure pattern. Both configurations show a strong wing trailing edge/sting shock in the leeward plane. For these angles of attack, windward trailing edge shocks were not present in the computations. The computations indicated an expansion of the leeward flow off the lower surface of the wing.

It should be mentioned that the grid is divided into two parts. The wing-body grid is used up to the end of the configuration. The grid is then regenerated on the sting and Mach cone surface as a simple polar grid. At the grid interface, the flow variables are interpolated from the wing-body grid onto the sting polar grid and the marching is continued.

Figures 11 and 12 show a sampling of the computed crossflow pressure patterns for the two configurations. Three crossflow stations are shown, the first approximately midway on the configuration, the second at the end of the configuration,

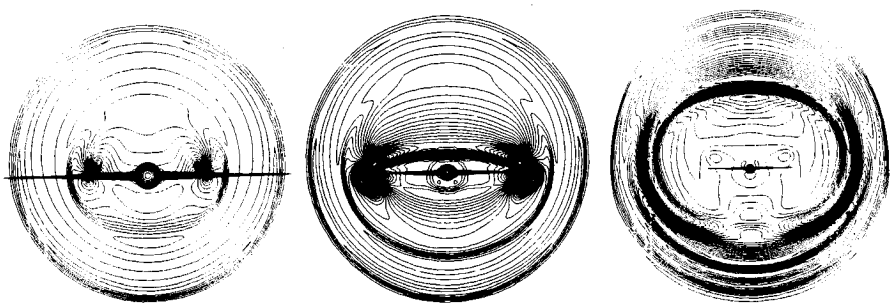

a) Midaircraft b) Aft end c) Body length downstream

Fig. 11 Selected crossflow plane pressure patterns for reference arrow wing-body configuration at $M_\infty = 2.70$, $\alpha = 2.75$ deg.

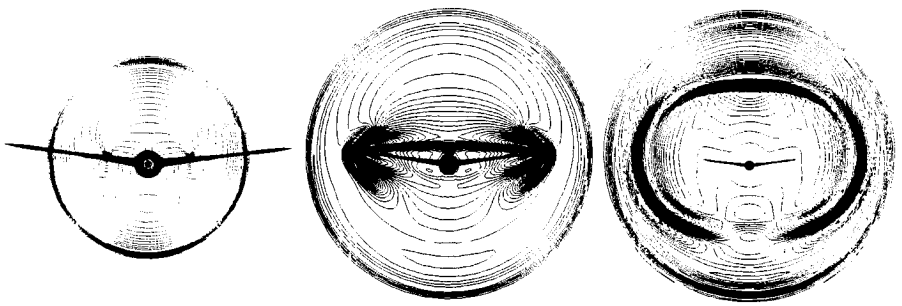

a) Midaircraft b) Aft end c) Body length downstream

Fig. 12 Selected crossflow plane pressure patterns for low-boom arrow wing-body configuration at $M_\infty = 2.70$, $\alpha = 2$ deg.

and the third station corresponding to roughly one body length downstream. At the first station, the reference configuration shows the bow shock and the wing emergence shock. At the aft end of the configuration, both configurations show wing trailing edge and wing crank shocks. Comparing Fig. 11b with 12b, the low-boom model shows only the bow or nose shock and a weak sting shock in the leeward plane. The patterns become more complex further downstream as indicated by Figs. 11c and 12c. It is interesting to note the circles above the wing tips in Fig. 12c. These are low-pressure areas generated by wing tip vortices. It should be noted that the set of pressure contour values used at each station is different.

Figure 13 shows a comparison between the measured wind-tunnel signatures and the computed sonic boom signatures for both configurations plotted vs full-scale coordinates in meters. Figure 13a shows the comparison for the reference configuration at 3.6 body lengths from the aircraft axis. The data were actually taken at a fixed distance from the model axis. The two different nondimensional distances are a result of the two different model lengths. The full-scale reference configuration was approximately 75-m long to the sting attachment point. Good agreement in the pressure signature is achieved up to the sting attachment. The nose shock and the wing emergence shock are in good agreement. The data show a third small shock persisting out to this distance, while the computation shows only a slight inflection in the pressure distribution. The computation used a simple cylindrical sting. The experimental data indicates a larger expansion in the sting region as compared to the computed results. A long sting was used in the wind-tunnel experiments and the model incidence was corrected to account for sting bending under load.

Figure 13b shows a comparison of the pressure signatures for the low-boom configuration. Excellent agreement between experiment and computation is achieved for the nose shock. The experimental data indicate a stronger wing emergence shock in comparison to the computed results. The experiment also shows a very strong third shock near the trailing edge of the configuration. The low-boom configuration is approximately 95-m long. The third shock shown in the experiment is of the same magnitude as the nose shock. The experiment also shows a larger expansion in the sting region as compared to the computed result. Also shown in Fig. 13b is the predicted low-boom signature as computed from sonic

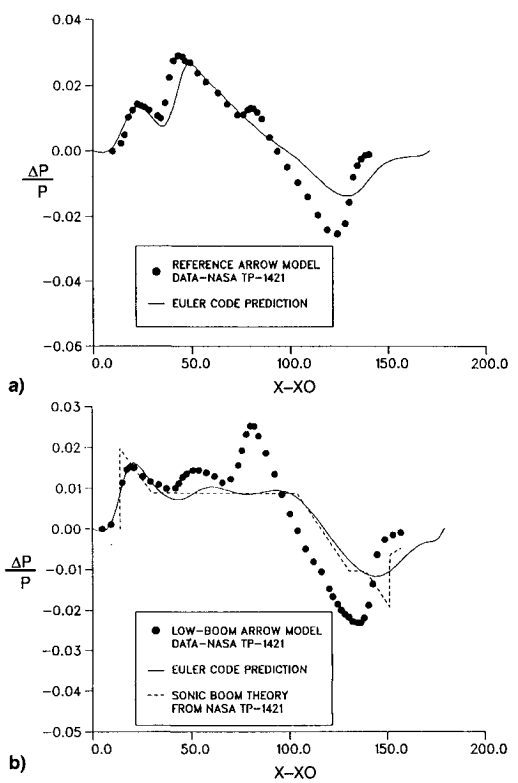

Fig. 13 Comparison of computed sonic boom signature with experimental data for the arrow wing-body configurations at $M_\infty = 2.7$: a) reference arrow wing-body configuration, $\alpha = 2.75$ deg, $H/L = 3.6$; b) low-boom arrow wing-body configuration, $\alpha = 2$ deg, $H/L = 2.9$.

boom minimization theory. The signature computed for the design geometry and the present results are in very good agreement. The authors of Ref. 8 were also surprised to see the discrepancy between predicted signature and measured data.

A variety of potential problems were illuminated. First, the published geometry corresponds to the models as designed, which was close to, but not entirely the same as, the wind-tunnel models that were constructed.[16] The actual geometry

of the models was not readily available. Building 4- to 5-in. models of a wing leads to a host of problems with accuracy, especially at the wing leading and trailing edges and the outboard panel of the wing, which are all very thin. Evidently, leading and trailing edges were blunted for practical purposes in model construction and also the wing outboard panel was thickened. Mack and Darden[8] were able to obtain the actual modified cross-sectional areas of the models. They also added cross-sectional area to account for viscous boundary-layer effects. A revised sonic boom theory signature corresponding to these effects was generated for the low-boom model in Ref. 8 and compared to the experimental data. Slightly better correlation was achieved, but there was still a large discrepancy at the third shock. It was postulated that further disagreement might be a nonlinear effect due to the high Mach number of 2.7 and the limitation of linear theory. As indicated in Fig. 13b, very good agreement is achieved between the present nonlinear computation and the sonic boom theory. The sonic boom theory slightly overpredicts the nose shock and shows a flat pressure signature up to the sting expansion. The present computation shows some nonlinearities in the region of the flat pressure. Hence, the present computation and the sonic boom theory are in relatively good agreement.

Figure 14 shows the experimental data plotted vs the computed sonic boom pressure signatures at several heights closer to the aircraft. Figure 14a corresponds to the reference configuration. The third shock absent in the computed results of Fig. 13a is indicated in the computed results at a third of a body length from the configuration. The computed results predict a rapid attenuation of this shock occurring at the aft end of the configuration. It is interesting to note that the signature changes very little in length over these distances. Figure 14b shows a similar plot for the low-boom configuration. At a quarter of a body length from the configuration, the third tail shock is present in the computed results. Once again, the computed results indicate a much weaker or a more rapid attenuation of this shock in comparison with the experimental data.

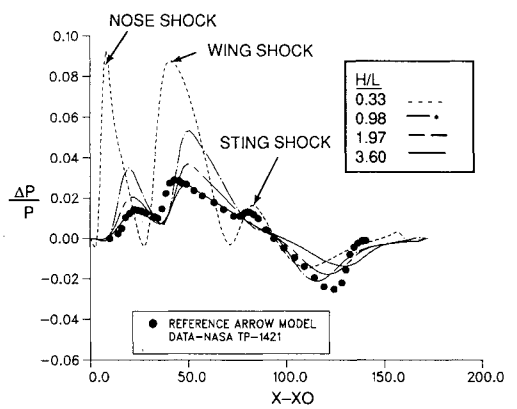

a) Reference arrow wing-body configuration, α = 2.75 deg

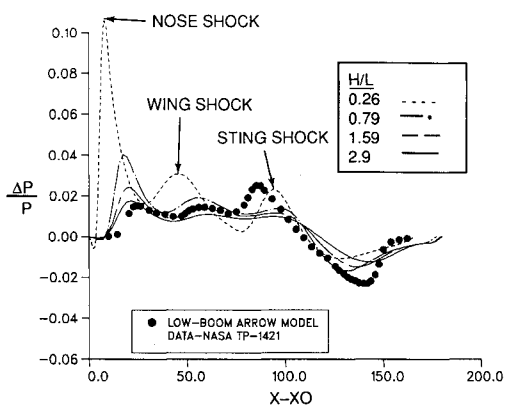

b) Low-boom arrow wing-body configuration, α = 2 deg

Fig. 14 Computed sonic boom signatures at various distances for the arrow wing-body configurations at M_∞ = 2.7.

The anomalous third shock in the measured signature has three possible sources: 1) the sting, 2) wing trailing edge, or 3) wing crank shock. There is also a complex interaction at the wing tips where a large expansion is generated as the leading edge turns parallel to the freestream. If experimental data were available at closer distances to the aircraft, it would be possible to determine the exact source of the discrepancy, which could merely have been modifications to the wing geometry that were made to the design geometry when the wind-tunnel models were built or due to significant boundary-layer effects.

Conclusions

A nonlinear Euler method has been applied to the computation of sonic boom pressure signatures in the near field to midfield for various Mach numbers. Good correlation was achieved for simple projectiles. The sonic boom signatures for two aircraft models were also computed at Mach 2.7 and incidence. Good correlation was achieved for the portion of the signature generated by the aircraft up to the tail shock. The tail shock and sting signatures were underpredicted by the present method. Further validation is required against experimental data with more attention given to the details of the actual geometry of the model.

References

[1]Whitham, G. B., "The Flow Pattern of a Supersonic Projectile," *Communications on Pure and Applied Mathematics*, Vol. 5, No. 3, 1952, pp. 301–348.

[2]Walkden, F., "The Shock Pattern of a Wing-Body Combination, Far from the Flight Path," *Aeronautical Quarterly*, Vol. 9, Pt. 2, May 1958, pp. 164–194.

[3]Hayes, W. D., Haefeli, R. C., and Kulsrud, H. E., "Sonic Boom Propagation in a Stratified Atmosphere, with Computer Program," NASA CR-1299, 1969.

[4]Siclari, M. J., "Nonlinear Analysis of Sonic Booms," Ph.D. Dissertation, New York Univ., New York, Jan. 1974.

[5]Ferri, A., Siclari, M., and Ting, L., "Sonic Boom Analysis for High Altitude Flight at High Mach Numbers," AIAA Paper 73-1034, Oct. 1973.

[6]Ferri, A., Ting, L., and Lo, R. W., "Nonlinear Sonic Boom Propagation Including the Asymmetric Effects," *AIAA Journal*, Vol. 15, No. 5, 1977, pp. 653–658.

[7]Darden, C. M., "An Analysis of Shock Coalescence Including Three Dimensional Effects with Application to Sonic Boom Extrapolation," NASA TP-2214, Jan. 1984.

[8]Mack, R. J., and Darden, C. M., "Wind Tunnel Investigation of the Validity of a Sonic Boom Minimization Concept," NASA TP-1421, Oct. 1979.

[9]Darden, C. M., "Study of the Limitations of Linear Theory Methods as Applied to Sonic Boom Calculations," 28th Aerospace Sciences Meeting, AIAA Paper 90-0368, Reno, NV, Jan. 1990.

[10]Siclari, M. J., "Hybrid Finite Volume Approach to Euler Solutions for Supersonic Flows," *AIAA Journal*, Vol. 28, No. 1, 1990, pp. 66–74.

[11]Siclari, M., "Three-Dimensional Hybrid Finite Volume Solutions to the Euler Equations for Supersonic/Hypersonic Aircraft," 27th Aerospace Sciences Meeting, AIAA Paper 89-0281, Reno, NV, Jan. 1989.

[12]Carlson, H. W., "An Investigation of Some Aspects of the Sonic Boom by Means of Wind Tunnel Measurements of Pressures About Several Bodies at a Mach Number of 2.01," NASA TND-161, Dec. 1959.

[13]Harvey, A. D., Acharya, S., Lawrence, S. L., and Cheung, S., "A Solution Adaptive Grid Procedure for an Upwind Parabolized Flow Solver," AIAA 21st Fluid Dynamics, Plasma Dynamics, and Lasers Conf., AIAA Paper 90-1567, Seattle, WA, June 1990.

[14]Nakahashi, K., and Deiwert, G. S., "Three Dimensional Adaptive Grid Method," *AIAA Journal*, Vol. 24, June 1986, pp. 948–954.

[15]Davies, C. B., and Ventatapathy, E. W., "A Simplified Self-Adaptive Grid Method, SAGE," NASA TM-102198, Oct. 1989.

[16]Mack, R. J., private communication, NASA Langley, Hampton, VA, July 1990.